Review of Scientific Instruments

RESEARCH ARTICLE | DECEMBER 07 2023

MiniMelt: An instrument for real-time tracking of electron beam additive manufacturing using synchrotron x-ray techniques

Hans-Henrik König ; Nick Semjatov ; Gabriel Spartacus ; Pidassa Bidola ; Chrysoula Ioannidou ; Jihui Ye ; Jakob Renner ; Ulrich Lienert ; Guilherme Abreu Faria; Benjamin Wahlmann ; Martin Wildheim ; Ulf Ackelid ; Felix Beckmann ; Peter Staron ; Peter Hedström ; Carolin Körner ; Greta Lindwall

Rev. Sci. Instrum. 94, 125103 (2023)
https://doi.org/10.1063/5.0177255

Review of Scientific Instruments ARTICLE pubs.aip.org/aip/rsi

MiniMelt: An instrument for real-time tracking of electron beam additive manufacturing using synchrotron x-ray techniques

Cite as: Rev. Sci. Instrum. 94, 125103 (2023); doi: 10.1063/5.0177255
Submitted: 20 September 2023 • Accepted: 15 November 2023 •
Published Online: 7 December 2023

Hans-Henrik König,[1,a] Nick Semjatov,[2] Gabriel Spartacus,[1] Pidassa Bidola,[3] Chrysoula Ioannidou,[1] Jihui Ye,[2] Jakob Renner,[2] Ulrich Lienert,[4] Guilherme Abreu Faria,[3] Benjamin Wahlmann,[2] Martin Wildheim,[5] Ulf Ackelid,[5] Felix Beckmann,[3] Peter Staron,[3] Peter Hedström,[1] Carolin Körner,[2] and Greta Lindwall[1,a]

AFFILIATIONS

[1] Department of Materials Science and Engineering, KTH Royal Institute of Technology, Brinellvägen 23, Stockholm SE-10044, Sweden
[2] Chair of Materials Science and Engineering for Metals, Friedrich-Alexander-Universität Erlangen-Nürnberg, Martensstr. 5, 91058 Erlangen, Germany
[3] Institute of Materials Physics, Helmholtz-Zentrum Hereon, Max-Planck-Str. 1, 21502 Geesthacht, Germany
[4] DESY Photon Science, 22607 Hamburg, Germany
[5] Freemelt AB, Bergfotsgatan 5A, SE-431 35 Mölndal, Sweden

[a] **Authors to whom correspondence should be addressed:** hhkonig@kth.se and gretal@kth.se

ABSTRACT

The development of a sample environment for *in situ* x-ray characterization during metal Electron Beam Powder Bed Fusion (PBF-EB), called MiniMelt, is presented. The design considerations, the features of the equipment, and its implementation at the synchrotron facility PETRA III at Deutsches Elektronen-Synchrotron, Hamburg, Germany, are described. The equipment is based on the commercially available Freemelt ONE PBF-EB system but has been customized with a unique process chamber to enable real-time synchrotron measurements during the additive manufacturing process. Furthermore, a new unconfined powder bed design to replicate the conditions of the full-scale PBF-EB process is introduced. The first radiography (15 kHz) and diffraction (1 kHz) measurements of PBF-EB with a hot-work tool steel and a Ni-base superalloy, as well as bulk metal melting with the CMSX-4 alloy, using the sample environment are presented. MiniMelt enables time-resolved investigations of the dynamic phenomena taking place during multi-layer PBF-EB, facilitating process understanding and development of advanced process strategies and materials for PBF-EB.

I. INTRODUCTION

Electron Beam Powder Bed Fusion (PBF-EB) is an Additive Manufacturing (AM) technology that utilizes an electron beam to selectively melt and fuse successive layers of metal powder to build up components. PBF-EB facilitates the processing of powders under vacuum (10^{-4}–10^{-5} mbar) and at high temperatures, reaching up to 1300 °C. Thereby, it enables the processing of refractory metals, high-temperature alloys, and nonweldable alloys.[1–3] Moreover, PBF-EB components exhibit reduced residual stress levels and consequently lower susceptibility to cracking when compared to components produced through the more prevalent Laser Beam Powder Bed Fusion (PBF-LB) process and its components.[4] Therefore, PBF-EB process development and materials research for PBF-EB are of great scientific and industrial interest.[5]

In PBF-EB, an electron beam is utilized as a high-energy heat source, with typical beam powers between 50 and 6000 W.[6] The PBF-EB process is described in Fig. 1. First, a start plate is heated up to the processing temperature with the electron beam. Once the processing temperature is reached, a series of process steps are

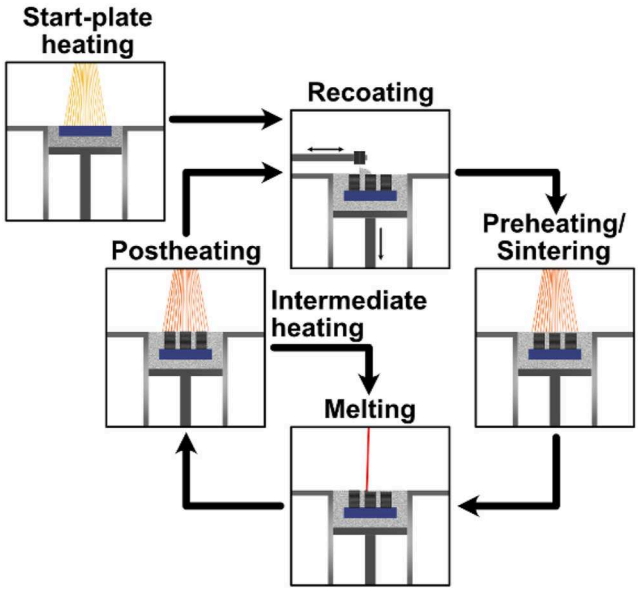

FIG. 1. Schematic of the typical process steps of the PBF-EB process. The start plate heating step is only used once at the beginning of the process, while the other steps are repeated for each layer until the build is finished.

iterated for each layer until the build is finished. At the beginning of each cycle, a thin layer of metallic powder (particle size distribution within the range of 45–150 μm[7]) is spread over the start plate (recoating). Subsequently, the powder layer is pre-heated to the processing temperature and weakly sintered to stabilize it against the so-called "smoke effect."[7] Afterward, the powder is selectively molten, followed by a post-heating step to ensure that the processing temperature is maintained. Depending on the number of components, it is also common to alternate between a melting and an intermediate heating step to maintain a more constant powder bed temperature. Finally, the build plate is lowered, and a new powder layer is applied. Through repetition of these steps, complex geometries can be produced by PBF-EB.[1,6] The process steps of PBF-EB induce transient thermal histories in the build components, as small melt pools (hundreds of μm) are created at very high scanning speeds (up to 10 km/s[7]) from which the material solidifies. Furthermore, the pre-, intermediate-, and post-heating as well as the spreading of new powder introduce changes to the temperature during the process. Through control of the thermal history during the process and through dedicated alloy design, locally controlled microstructures can be achieved,[1] enabling optimization of the mechanical properties within components.[1,8]

To facilitate alloy and process development for PBF-EB, a fundamental understanding of the governing physics of heating, melting, and solidification cycles is necessary.[6] Various models have been developed to link process parameters to the resulting microstructures and to describe the interactions between the physical phenomena underlying PBF-EB.[5,8] Combined with experimental observations, these models can be powerful tools for alloy design and process strategy development for PBF-EB.

Profound insights into PBF-LB have been revealed by *in situ* synchrotron x-ray techniques, including radiography, Wide-Angle X-ray Scattering (WAXS), and Small-Angle X-ray Scattering (SAXS).[9] These techniques provide real-time experimental information on PBF processes at high spatial (tens of μm) and temporal resolutions (up to MHz).[9] Real-time synchrotron measurements have been applied to study transient phenomena such as melt pool dynamics,[10] pore formation,[11] cracking,[12] solidification,[13] phase transformation,[14] precipitation,[15] and stress formation[16] during the PBF-LB process. These measurements unveiled the dynamics of the listed phenomena, enabled their classification, and validated computational models of the laser heat source[17] and rapid solidification.[18–20] The advances in the fundamental understanding of dynamic phenomena during PBF-LB were made possible through the implementation of several *in situ* synchrotron sample environments for PBF-LB at various synchrotron sources.[9]

Although PBF-LB and PBF-EB are conceptually similar, there are significant differences between the techniques, related to the nature of the heat sources, the process steps, and the different processing environments. For instance, the underlying reflection and absorption mechanisms of electrons and photons on the surface of the processed material are distinct and result in electron beam penetration depths in the range of 10^1–10^2 μm, whereas laser beams only reach a penetration depth of tens of nm.[7] These differences in the depth of material interaction between electron and laser heat sources, the energy deposition efficiencies, and the different processing environments (vacuum for the electron beam compared to an inert gas atmosphere for the laser) lead to different melting and evaporation dynamics. Furthermore, the smoke effect, which is assumed to be induced by electrostatic charging of particles by the electron beam, leading to particle ejection and powder bed destruction, is process-specific and only occurs during PBF-EB.[7] In addition, the higher process temperatures in PBF-EB result in different thermal conditions and, therefore, lead to different solidification and phase transformation conditions. Until now, only one sample environment for PBF-EB has been presented by Escano *et al.*,[21] but no sample environment that allows for replication of the full PBF-EB process cycle at a synchrotron source has been developed and communicated. This may be attributed to the challenges involved in developing an experimental setup for *in situ* synchrotron studies of PBF-EB, i.e., a suitable (high power) electron beam source and a vacuum chamber capable of withstanding high temperatures.

The powder bed, in particular, is of high importance in the design of the sample environment to ensure both good observability by synchrotron x-ray measurements and accurate representation of the real PBF process. The powder bed design has a crucial influence on the thermal conditions that will prevail in the sample during *in situ* observations.[20] The thermal conditions are a major cause not only for the formation of AM-specific microstructures but also for the occurrence of defects in AM.[5] The first presented PBF-LB *in situ* sample environment by Zhao *et al.*[22] utilized a thin layer of powder on top of a Ti6Al4V plate sandwiched between two glassy carbon plates. This sandwich-type powder bed design has been used and further refined in several other PBF-LB sample environments.[23,24] Uhlmann *et al.*[25] constructed a sample environment that allows powder layers to be recoated and multi-layer sandwich-type samples to be measured. The sandwich-type powder bed design enables the investigation of a slice of the powder bed and melt pool during PBF. However, this method comes with the limitation that the x-ray transparent plates act as boundaries to heat diffusion as well as

to the three-dimensional flow of the melt pool, compared to industrial processes. In particular, direct contact between the melt pool and the x-ray transparent plates modifies the processing conditions significantly, particularly the melt pool dynamics. Consequently, the transferability of observations from sandwich-type sample environments to industrial processes may be a concern. A miniaturized PBF-LB device has been presented by Hocine *et al.*[26] that addresses this concern. The device enables the processing of multi-layer 3D samples on a 12 × 12 mm^2 build plate and complex scanning strategies. Recently, diffraction and radiography experiments have been performed with a sample environment for *in situ* electron beam melting by Escano *et al.*[21] A bare Ti6Al4V plate and a prefabricated Ti6Al4V substrate with sintered powder were used for melting experiments.

To address the need for an *in situ* PBF-EB sample environment, we present the MiniMelt, a PBF-EB system for *in situ* studies capable of performing a full multi-layer PBF-EB process in a synchrotron experiment. Furthermore, we introduce an unconfined powder bed design, enabling measurements of a specific section of the powder bed during the PBF-EB process, aiming at representing the thermal conditions of the real PBF-EB process. In the following, the development and design of the equipment are detailed, and the first results of *in situ* radiography and diffraction of the PBF-EB process utilizing this environment are presented.

II. INSTRUMENT DESIGN

A. Design criteria

The sample environment MiniMelt is designed to replicate the full PBF-EB process while enabling *in situ* x-ray measurements in a synchrotron environment (see Fig. 2). Therefore, the sample environment needs to allow the synchrotron x-ray beam to enter and exit the process chamber during processing. Furthermore, the size and weight of the equipment have to be compatible with the Swedish Materials Science beamline P21.2 (for diffraction and small-angle scattering experiments) and the White Beam Engineering Materials Science beamline P61A (for white beam radiography experiments) of the PETRA III synchrotron. In addition, the thermal conditions within the miniaturized powder bed need to be similar to the industrial process to ensure that the gained knowledge is transferable to an industrial-scale PBF-EB process (Sec. II D, unconfined powder bed). The equipment's software (Sec. II C, software) has to ensure detailed machine and process control for a flexible design of experiments, provide data collection capabilities during the experiments

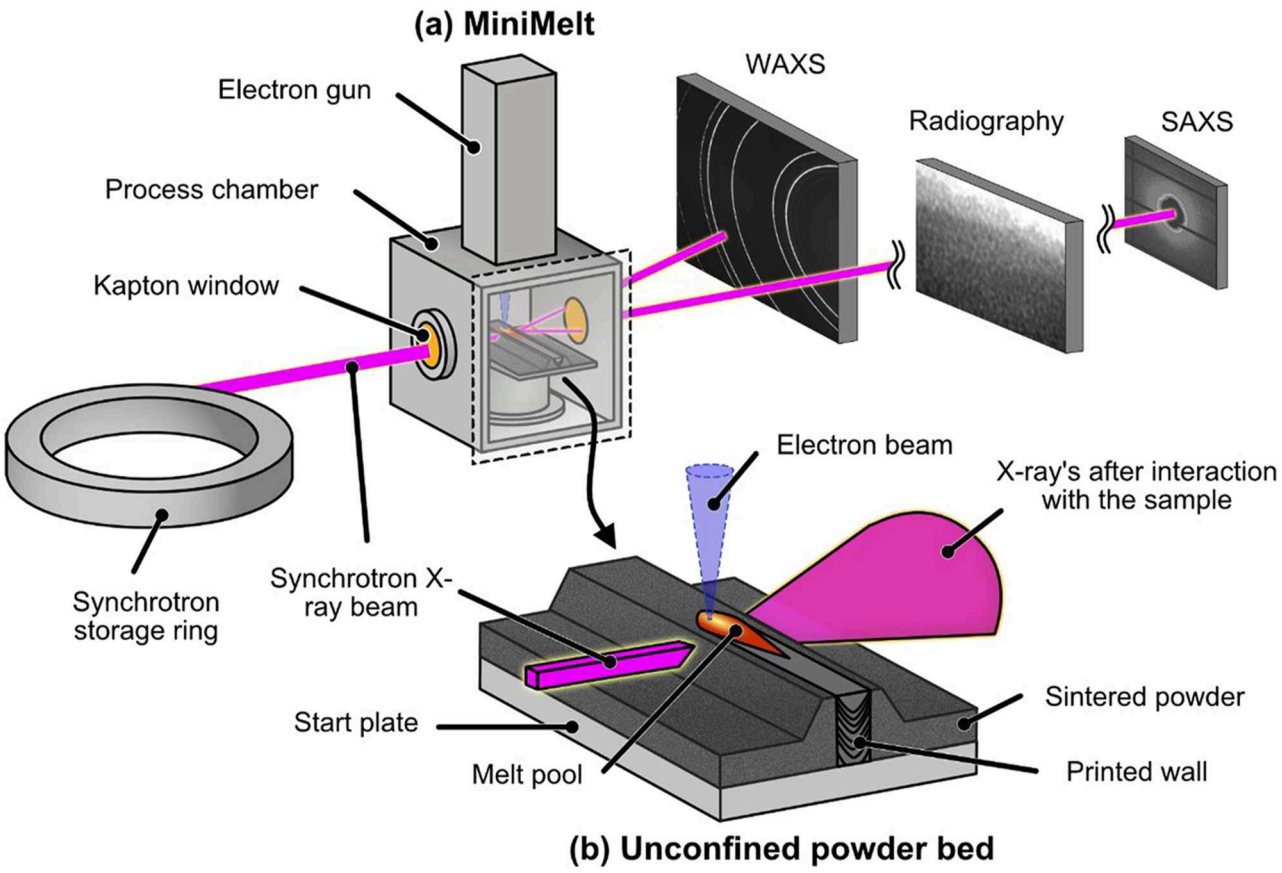

FIG. 2. (a) Schematic of the PBF-EB experimental setup (MiniMelt) for measurements of Wide-Angle X-ray Scattering (WAXS), radiography, and Small-Angle X-ray Scattering (SAXS) in a synchrotron. (b) Schematic of the unconfined powder bed where the x-ray beam interacts with the sample.

through the sensors of the equipment, and allow synchronization of the process with the radiography and diffraction detectors.

B. Equipment specifications

MiniMelt is based on the commercially available Freemelt ONE system by Freemelt AB (Mölndal, Sweden). Freemelt ONE is a freely programable PBF-EB machine developed for research applications.

The main components of the sample environment include an electron gun, turbo pumps, a process chamber, a viewport, x-ray transparent windows, and a recoater system [see Fig. 3(a)]. These components are mounted inside an aluminum frame to allow transportation and positioning of the equipment. For lifting, rotatable lifting eyes are attached at the top of the frame. The dimensions of the sample environment are 1180 × 660 × 1600 mm^3 (length × width × height), and the weight is 365 kg, excluding the weight of the control unit that can be placed separately. The distance from the bottom of the sample environment frame to the measurement position is 350 mm.

The electron gun is the same type of gun used in the Freemelt ONE system: a diode-type source with a laser-heated cathode (LaB_6). The acceleration voltage is 60 kV, and the electron beam power can reach up to 6 kW. The coils in the beam-column are shaping, focusing, and deflecting the electron beam at velocities of up to 10^5 m/s. Beam sizes of less than 250 μm full-width half power (FWHP) can be reached. Two turbomolecular pumps (Turbovac 90i, Leybold GmbH, Köln, Germany) sustain a vacuum of 10^{-4} to 10^{-5} mbar during the process. A magnetic valve to introduce inert gases for cooling after the build process is completed is installed on the vacuum pump attached to the electron gun chamber.

Two x-ray transparent windows made of Kapton® 500HN (127 μm) are attached to the process chamber, and one window is located on the chamber door [Fig. 3(c)] and the other window is located on the backside of the chamber. These windows have a diameter of 66 mm and allow for collecting diffraction angles of up to 14°. The x-ray windows are attached with copper-sealed CF100 flanges to the process chamber and can be replaced with blind flanges that eliminate radiation leakage (generated by electron beam—material interaction) to allow safe operation outside

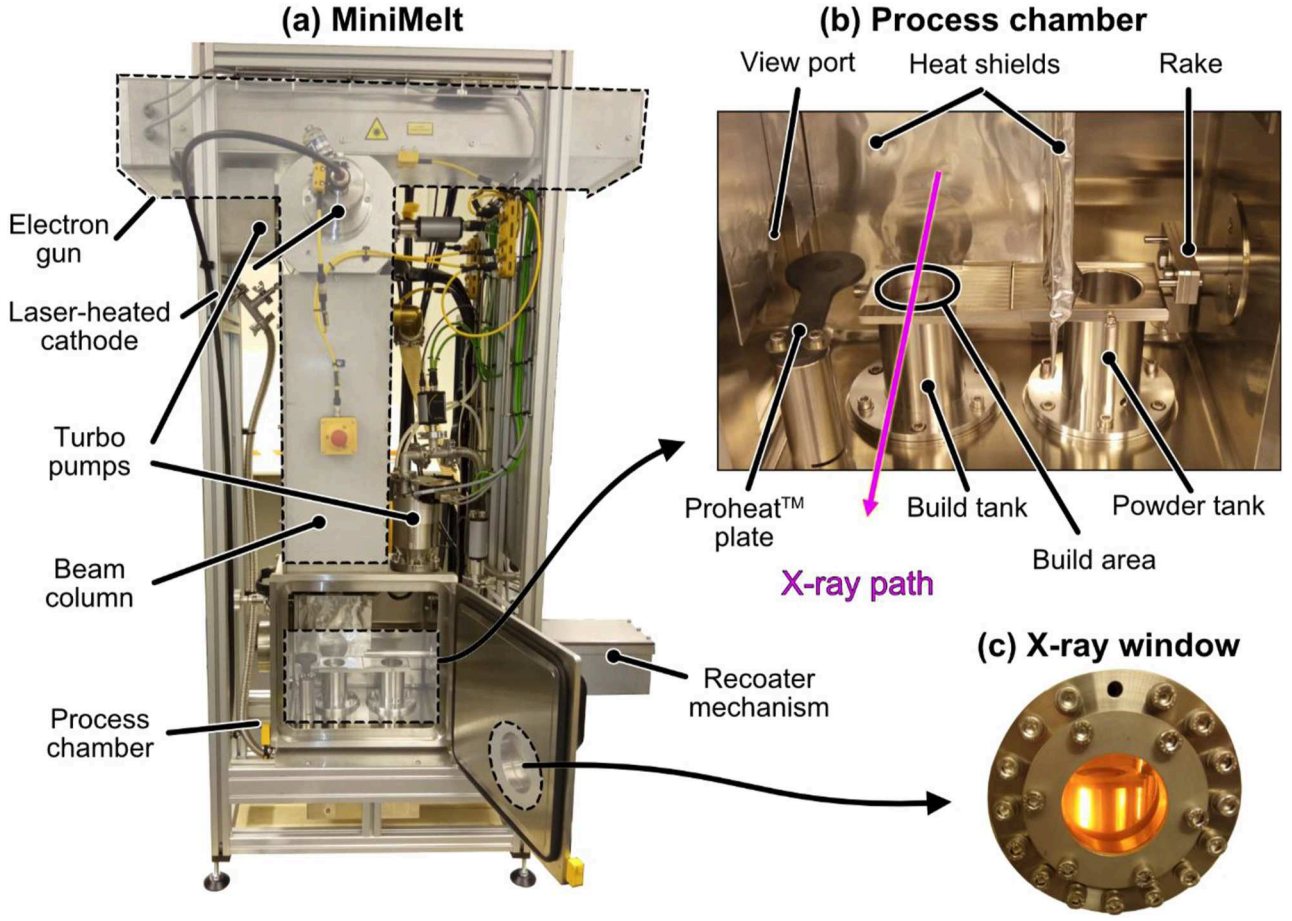

FIG. 3. (a) Image of the sample environment (MiniMelt) with the main components indicated. (b) The inside of the process chamber where the PBF-EB process takes place. (c) The x-ray window is made from Kapton.

experimental hutches. The sample environment is equipped with a safety interlock system that controls the high-voltage unit. The interlock system includes various switches on the process chamber doors, the cathode chamber, the laser housing, and two emergency stop buttons on the machine. The interlock of the machine can be connected to the beamline's interlock system to ensure safe operation. These features allow us to operate MiniMelt in two modes: In mode 1, the Kapton windows are installed to allow synchrotron x rays to interact with the sample inside the process chamber. In mode 2, the blind flanges are installed, and operation in a lab space, e.g., process parameter development, is possible.

The interior of the process chamber is shown in Fig. 3(b), including the build area, where the interaction of the x-ray beam and the powder bed occurs. The process chamber contains all components necessary for a layer-by-layer PBF process. These include a build and a powder tank with movable tables (diameter of 50 mm, effective height of 50 mm, and a volume of 98 cm^3), the recoater, and heat shielding plates. The internal volume of the process chamber is 21 000 cm^3, much smaller than the process chamber volume of Freemelt ONE, which is 70 000 cm^3. The process chamber has 20 mm thick stainless-steel walls and provides four DN 40 ports that can be used to connect additional sensors and other accessories.

The powder recoating system in MiniMelt is a linearly moving recoater. The recoater transports the powder from the powder tank to the build tank and creates a powder layer of adjustable thickness in the build area. This design differs from the more common funnel-based powder feeding systems that are used in *in situ* synchrotron PBF-LB devices.[25,26] The linear moving recoater of MiniMelt is based on the powder feeding system of the Freemelt ONE and reduces powder flowability issues.

Inside the vacuum chamber, a movable graphite plate is installed, the ProHeat^{TM} plate. This graphite plate can be swiveled to the build area over the powder bed and heated by the electron beam. The ProHeat plate can thereby provide heating to the powder bed by thermal radiation without introducing an electric charge into the powder bed.[27]

The control unit of the sample environment is mounted on a metal EUR-pallet and houses the electrical cabinet, the high voltage unit, the control computer, the beam control unit, as well as a ventilation fan for cooling the beam-column. Furthermore, MiniMelt includes a closed liquid cooling system for the cathode heating laser and the turbopumps.

In addition, the synchrotron-based measurements (WAXS, SAXS, and radiography), the sample environment includes several sensors that provide data for process monitoring. The temperature below the start plate is monitored using a type N thermocouple. In total, four feedthroughs for thermocouples into the process chamber are available. Two pressure sensors are used to monitor the pressure inside the system. One pressure sensor is attached to the process chamber, and the other one is attached to the electron gun chamber. A webcam is used to get live images through the viewport from the process chamber and the build area. A four-segment total electron emission (TEE)[28] detector [often referred to as a backscattered electron (BSE) detector] is installed at the top of the process chamber, surrounding the electron beam entrance to the chamber. This TEE-detector is used for calibration and characterization of the electron beam, to record ELectron-Optical (ELO) images,[29] and to provide *in situ* data that can be used for in-process monitoring.[30] The ELO imaging system is utilized to determine the sample positions inside the build chamber and to align the melting locations with the x-ray beam during synchrotron experiments (Sec. II C 2, ELO imaging).

C. Software

Since MiniMelt is based on the Freemelt ONE system, the machine control software is the same as found on that system. This includes a software interface to control the various components of the machine (called BOCCI) as well as the backend, supporting beam deflection control, beam calibration, log data acquisition, TEE signal collection, and other features. Similar to standard Freemelt ONE machines, MiniMelt is freely programmable and does not come with preinstalled proprietary software for build file creation or TEE-based process monitoring. Consequently, appropriate software had to be developed, implemented, and tailored toward the requirements of an *in situ* PBF-EB sample environment. This includes the capability of the machine to communicate with the beamline detectors when to record data based on pre-programmed user input, i.e., a triggering system.

1. Build file creation

On PBF-EB machines made by Freemelt, scan objects (such as points, lines, and curves) can be defined by the user via an openly available Python package called *obplib*. Since a build process that

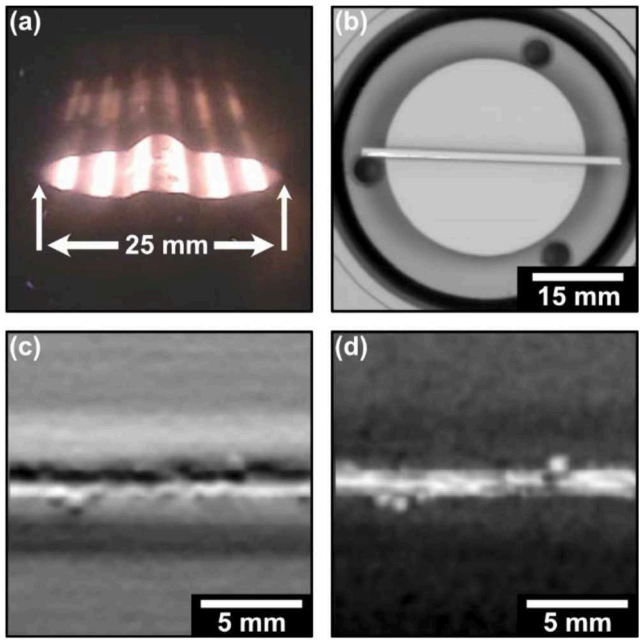

FIG. 4. Example images of the process monitoring capabilities of the MiniMelt system. (a) Shows a snapshot of a video recording of a powder build using a webcam via the viewport. (b) Shows an ELO image (in material/density contrast mode) of a bulk sample inside the build tank (used for beam path positioning), while (c) and (d) show ELO images of a single line melt within the unconfined powder bed in topography and density contrast mode, respectively.

maps all the process steps of PBF-EB requires thousands of these individual "obp-objects," a Python-based software called Procsisem (process control software for *in situ* EBM machines) was developed specifically for the needs of MiniMelt. The software contains a library of functions that describe the various scan objects required to perform a complete PBF-EB process. These include functions for the creation of heating files for initial start-plate-, pre-, and post-heating, as well as melt figures and additional support patterns, such as functions to embed markers for various trigger events within the pattern files. A compiler converts a user-defined selection of these functions and the necessary scanning parameters (such as velocities, beam powers, spot sizes, and scanning strategies) for each function into a full, multi-layer build. The software allows for easy implementation of new pattern functions and has a built-in feature that coordinates beam power changes between individual patterns. It is thereby ensured that melting and heating patterns are executed at their targeted power values (accounting for the time the cathode needs to adjust to a new beam power target value). Finally, the software allows us to change almost all process parameters during a running build process without interruption.

An essential feature of the MiniMelt system and the Procsisem software is the ability to predefine within compiled build files when beamline detectors are supposed to record a measurement. This is realized through Freemelts' Syncpoint feature (part of *obplib*). By placing Syncpoints within the beam pattern files, the user can accurately define when to trigger a specified event on a Freemelt system. MiniMelt can detect such a Syncpoint during a process and output a 5 V TTL signal, which can be used to trigger detectors. The recording of TEE signals from the four-segment TEE detector during the process can be similarly triggered via a different Syncpoint. Both trigger signals are implemented as functions within Procsisem.

Procsisem is compatible with MiniMelt and other Freemelt ONE systems, allowing users to test build procedures and new code implementations on a standard Freemelt ONE system before performing experiments at a synchrotron.

2. ELO imaging

Utilizing the signals from the TEE detectors, MiniMelt can be used to create ELO images. This functionality is required to locate samples inside the process chamber and can also provide information about the surfaces and objects in the build area during the process. To create ELO images, the working principle of scanning electron microscopes is applied. The time series intensity data collected by the TEE detectors during a raster scan is combined with beam position data to render ELO images [Figs. 4(b)–4(d)].

The ELO imaging is realized by a Python-based ELO imaging software (FreemeltELO) that was initially developed for TEE-based process monitoring on Freemelt ONE systems. An example of the process monitoring capabilities of this software on a Freemelt ONE system can be found in a publication by Bäreis *et al.*[29] The software allows us to define imaging settings, including the position and size of the scanning area, and to perform an ELO scan at the end of each layer during a build process. To achieve that, the software interacts with the backend of the MiniMelt system to automatically pause a running build process at the end of each layer and record an image before continuing the build process with the recoating. The images recorded by each of the four detectors, as well as topography and material contrast images (through subtraction and addition of opposing detectors, respectively), are displayed in a graphical user interface. In addition, the software provides the ability to manually caputre images of a scanned surface outside of the build process. While the automated process monitoring mode is mainly used to monitor changes during a running build process, the manual mode

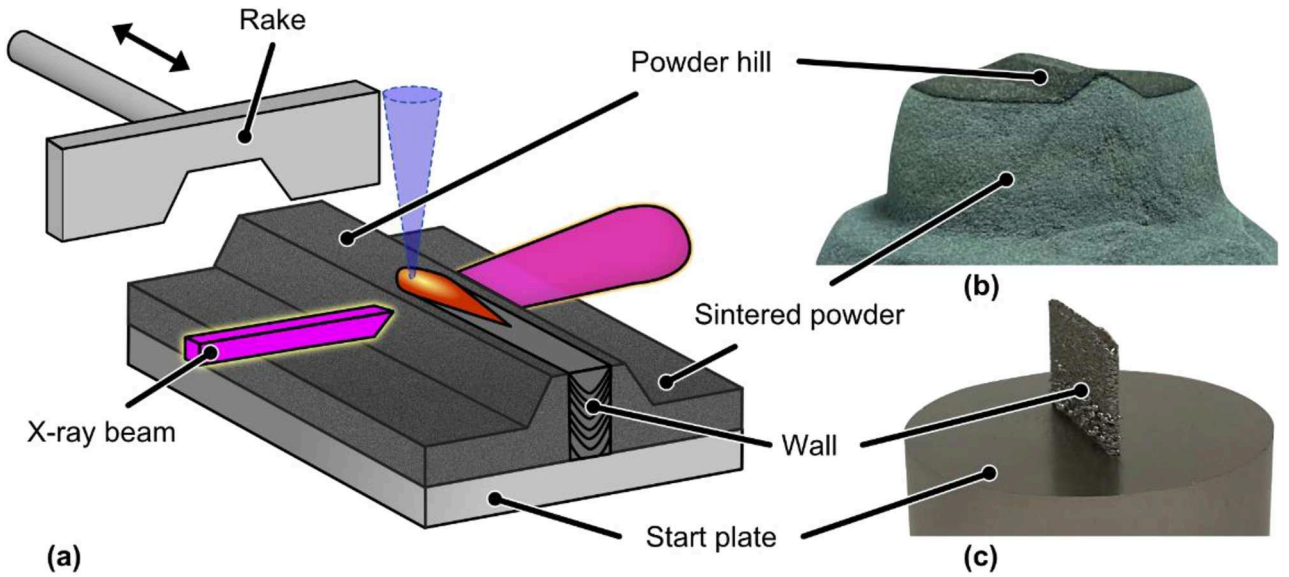

FIG. 5. The unconfined powder bed. (a) Schematic of an *in situ* measurement with the unconfined powder bed. (b) A sinter cake with an incorporated wall, processed with MiniMelt. (c) A manufactured wall on top of a start plate, processed with MiniMelt (sinter cake removed).

is used to record images of bulk samples and remelting experiments, determine the positioning of installed samples, and define the scanning paths of the electron beam. Examples of the various process monitoring and imaging modes are displayed in Fig. 4. The manual recording of bulk samples inside the build tank is an essential tool to make experiments with bulk samples possible.

D. Unconfined powder bed

A new unconfined powder bed design was developed in conjunction with the MiniMelt to ensure the observability of the PBF-EB process with synchrotron techniques (radiography and scattering) while being as representative as possible of the industrial PBF-EB process. In this design, the powder bed is shaped during the layer-wise build process by modified rake blades with a trapezoidal cutout (see Fig. 5). The pre-heating step unique to PBF-EB allows us to stabilize the trapezoidal shape during the build process.

The geometry of the trapezoidal powder hill (height of 2 mm, a top width of 1 mm, and an inclination angle of 35°) was determined during preliminary studies. The inclination of the hill is small enough to not exceed the flowability limit of standard PBF-EB powder (spherical, size distribution between 45 and 105/150 μm), whereas the top width of 1 mm ensures that a single melt line or similarly small sample sizes remain surrounded by powder. The powder surrounding the melt pool ensures that melt pool dynamics during melting and thermal diffusion during and after melting remain representative of an industrial scale PBF-EB process (according to thermal diffusion simulations performed with CMSX-4 as a model material[31]), different from sandwich-type powder bed designs where the melt pool tends to get in direct contact with the x-ray transparent walls.

The powder hill is created automatically layer by layer at the beginning of the build process (first ~20 layers) on top of the start plate until the target height, defined by the rake blade design, is reached. The geometry of the powder hill can be varied by mounting rake blades with different cutout designs. The unconfined powder bed design not only allows for single-line scans but also for the processing of three-dimensional melt patterns.

In addition to the unconfined powder bed, the relatively large build tank (50 mm diameter) provides enough space for bulk samples to be positioned, while the FreemeltELO software allows the users to target the sample with the electron beam reliably.

III. SYNCHROTRON X-RAY MEASUREMENTS

MiniMelt is compatible with the Swedish Materials Science beamline P21.2 and the High Energy Material Science beamline P61A of the synchrotron PETRA III at DESY, Hamburg. During commissioning beamtimes, *in situ* WAXS and SAXS experiments with a monochromatic beam and radiography experiments with a white beam were performed. An overview of the first results captured during these commissioning beamtimes at both beamlines is provided in Secs. III A and III B.

A. Radiography at P61A

The *in situ* radiography experiments at high frame rates (up to 15 kHz) were performed using a white beam (40–200 keV) of the size 2.5 × 1.5 mm^2 (width × height). The transmitted beam was converted into visible light using a cerium-doped gadolinium gallium garnet (GaGG:Ce) scintillator (400 μm, actively cooled using N_2 gas). A focusing lens assembly and 45° reflection mirrors are part of the radiography system. The images were magnified with an objective lens with 10× magnification power and recorded on a high-speed camera (Phantom v2640, Vision Research, USA). The maximum recorded resolution was 2048 × 1952 pixels, with an effective pixel size of 1.35 μm. Before the sample, various attenuator materials (copper, aluminum, iron, tantalum, and tungsten) were introduced into the incident x-ray beam to vary its intensity and energy bandwidth. The selection of attenuator materials and their respective thicknesses was informed by simple absorption calculations and trial-and-error testing. The attenuators mitigated the thermal load on the scintillator while simultaneously optimizing the x-ray energy bandwidth and thereby enhancing the contrast during imaging of the samples. Notably, the high absorbance of the CMSX-4 samples required attenuation to harden the x-ray beam and reduce the thermal load on the samples. The radiography setup is presented in Fig. 6, and more details can be found in Bidola *et al.*[32]

In Fig. 7, several radiography frames recorded during the melting of a line in the unconfined powder bed at 6.6 kHz are displayed. During these measurements, 10 mm Al and 200 μm Ta were used as attenuators. The processed material was a hot-work tool steel with the composition listed in Table I, provided by Uddeholm AB, Sweden. The particle size distribution of the tool steel power was 50–150 μm.

The electron beam was scanned from left to right at a velocity of 200 mm/s with a power of 240 W. During scanning, the powder was melted and densified, and the top surface of the built wall was therefore located below the top of the powder hill surface, as illustrated in Fig. 7(a). In Figs. 7(b) to 7(e), the gray values are directly correlated with the x-ray transmission of the material and, hence, to the electron density. Figures 7(a′) to (e′) show the difference between the frames before the arrival of the electron beam on the field of view

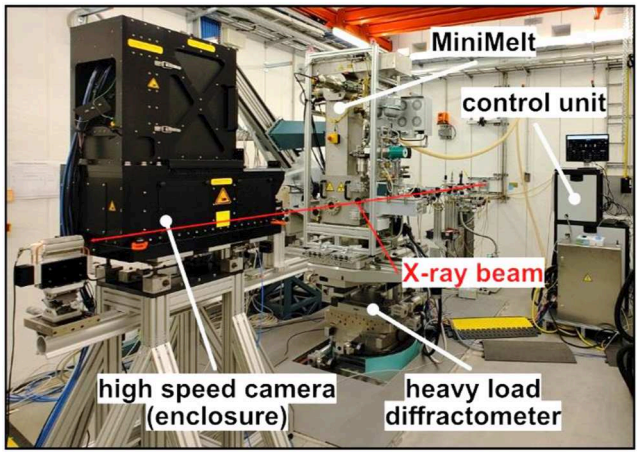

FIG. 6. Radiography setup at beamline P61A. The MiniMelt is placed on a heavy load diffractometer, allowing for positional adjustments in the x-, y-, and z-directions. The high-speed camera is protected from radiation by an enclosure, which provides 25 mm of lead shielding.

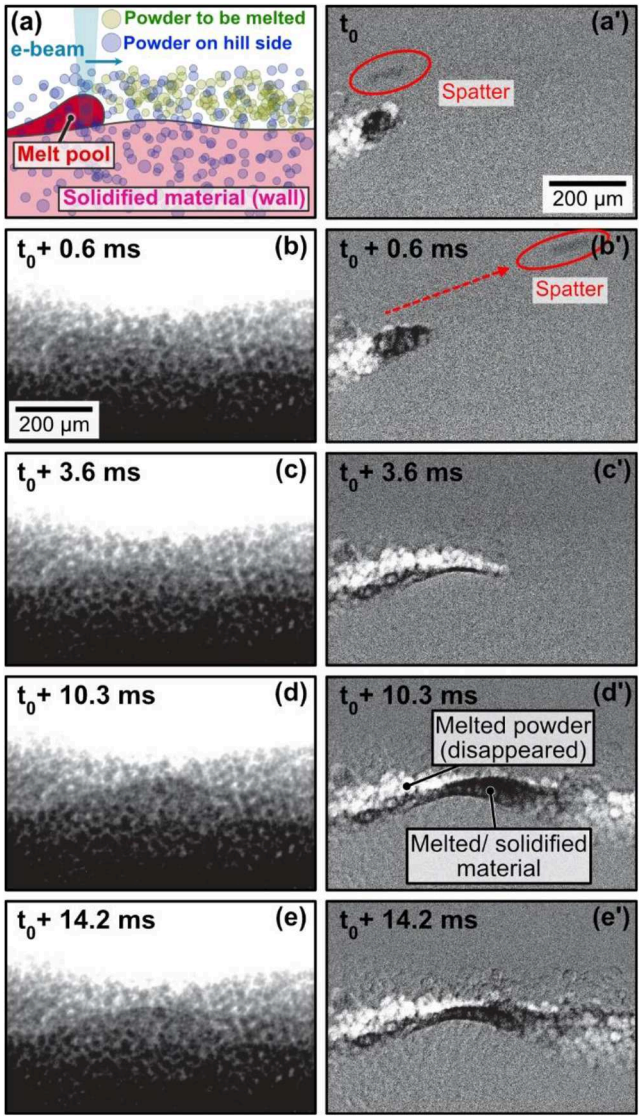

FIG. 7. *In situ* radiography showing the PBF-EB process of tool steel during the melting of a line in the unconfined powder bed. Schematic of the process (a), radiography density contrast at different times (b) to (e), and density evolution over the melting showing the molten material (in dark) and the disappeared powder particles (in white) at different times (a′) to (e′) (multimedia available online).

and the current frame, exhibiting the evolution of the x-ray transmission (related to the material's density) within the field of view. With this image processing, the melted or solidified material (dark, due to the density increase) and the melted powder particles (light, due to the density decrease) can be identified. Furthermore, the melt pool depth can be quantitatively retrieved, as can the molten metal flow (not presented here). In Figs. 7(a′) and 7(b′), an ejected spatter particle is visible, allowing us to estimate its velocity, size, and direction.

Figure 8 displays a series of radiography frames exhibiting the smoke effect. For this experiment, a steady electron beam with a

TABLE I. Nominal composition of the steel powder in mass-%.

Element	Fe	C	Cr	Mo	V	Mn	Si	N
Composition [mass-%]	Bal	0.35	4.93	2.24	0.54	0.45	0.25	0.049

beam power of 60 W and a dwell time of 30 ms was targeted at the powder bed at room temperature [displayed in Fig. 8(a), showing the top of the powder hill]. The images were recorded at 6.6 kHz with 10 mm Al and 200 µm Ta attenuators. The utilized powder was a Ni-base superalloy, EIGA atomized (by TLS Technik GmbH & Co. Spezialpulver KG, Bitterfeld, Germany) from CMSX-4 feedstock rods (Ross & Catherall Ltd., Sheffield, UK). The powder has a spherical morphology and a particle size distribution of 45–105 µm.

When the electron beam hits the powder bed, a melted material aggregate forms [Fig. 8(b)]. As the beam continues to hit the same spot, the powder particles surrounding the electron beam position are repelled to the sides, setting more and more particles in motion [Figs. 8(c) and 8(d)]. In Figs. 8(e) and 8(f), all powder particles are rapidly accelerated out of the powder bed due to electrostatic repulsion.

Aside from powder bed experiments, the MiniMelt can also be used for electron beam remelting experiments on thin bulk samples. This is demonstrated in Fig. 9, where an electron beam was scanned

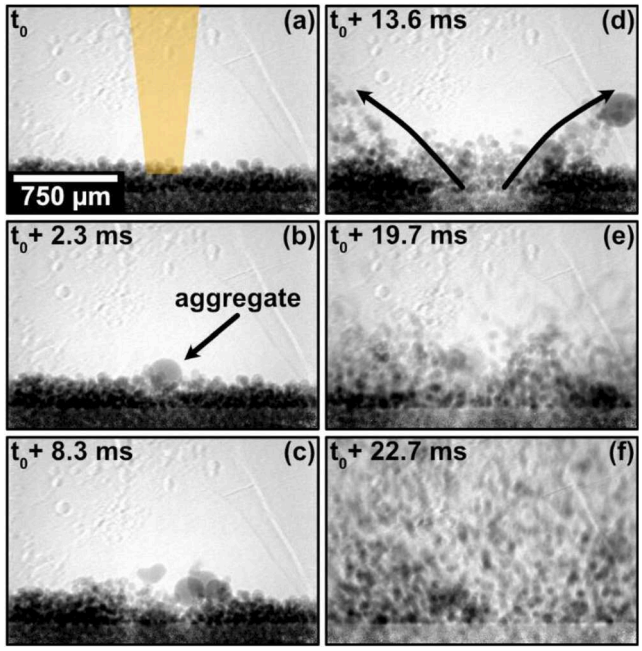

FIG. 8. X-ray radiography time series of the smoke effect, showcasing melting, charge up, and electrostatic repulsion due to a standing electron beam. (a) Turning on the electron beam on the sample surface (dwell time: 30 ms), (b) formation of a melted material aggregate, (c) and (d) evaporation driven repulsion of particles from the beam impact area, (e) and (f) rapid repulsion of powder particles from the powder bed due to electrostatic discharge of charged-up powder particles.

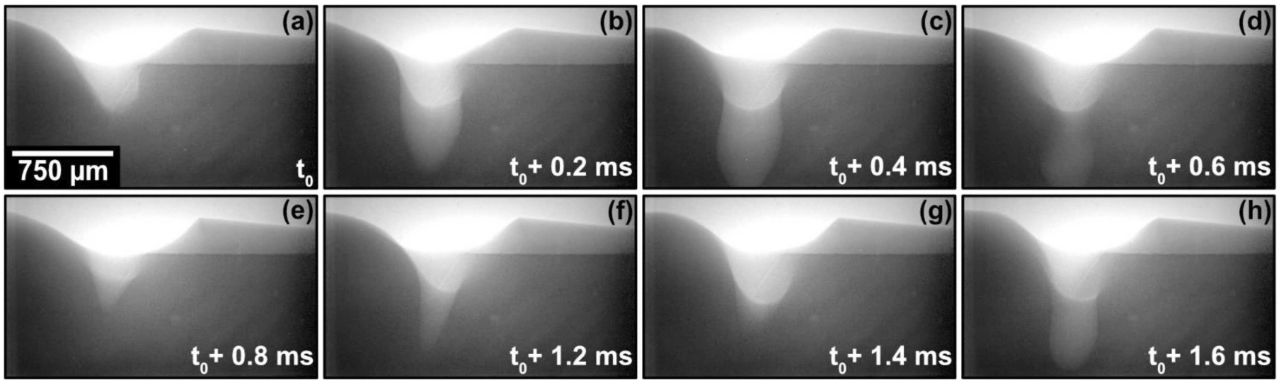

FIG. 9. *In situ* radiography of electron beam melting of a 1.1 mm thick bulk CMSX-4 sample, recorded at 15 kHz. Creation and expansion of a keyhole due to evaporation driven recoil pressure (a) to (c). Collapse of the keyhole (d) and (e). Recreation of the keyhole (f) to (h) [similar to (a) to (c)]. Overall periodic formation and collapse of a keyhole.

over a 1.1 mm thick (in x-ray beam direction) bulk CMSX-4 sample at room temperature using a beam power of 560 W and a scanning velocity of 25 mm/s. The images were recorded at an acquisition rate of 15 kHz and showcased the formation of an oscillating keyhole moving through the sample while reaching a melt pool depth of over 1 mm. The same attenuators as in the smoke experiment were used.

In addition to the presented measurements, the MiniMelt and high-speed radiography at P61A are also expected to allow for insights on powder behavior and flowability during powder raking depending on the powder characteristics, powder sintering behavior depending on the pre- and post-heating parameters, crack formation and growth, as well as pore formation.

B. X-ray scattering at P21.2

Simultaneous SAXS and WAXS measurements were performed at the P21.2 beamline (setup in Fig. 10). A monochromatic x-ray beam of 68 keV (energy resolution of $\Delta E/E = 10^{-3}$) and a beam size of 0.1×1 mm^2 (width × height) were utilized. The width of the x-ray beam was optimized to ensure a sufficient x-ray flux while providing a sufficient spatial resolution in the direction of the electron beam travel. The center of the x-ray beam was positioned at the top of the powder hill, so that ~ 0.5 mm of the beam height was inside the unconfined powder hill, giving rise to the SAXS/WAXS signal. The WAXS signal was recorded with an EIGER2 4M detector (frame rate up to 1.12 kHz) placed at a sample-to-detector distance of ~ 1 m. To record the SAXS signal, a Pilatus 2M detector with a frame rate capability of 500 Hz was utilized at a sample-to-detector distance of ~ 15 m. The SAXS signal was guided through an evacuated flight tube to reduce air scattering. The 2D images were azimuthally integrated using LaB6 and AgBh calibration samples for the WAXS and the SAXS data, respectively. The azimuthal integration was performed on the Maxwell HPC cluster at DESY with a Python script applying the pyFAI[33] package. This script is capable of an integration time of ~ 22 ms per frame of an EIGER2 4M and ~ 9 ms per frame of an EIGER2 1M, enabling online data visualization for datasets typically consisting of around 10 000 frames.

WAXS data were recorded during PBF-EB of a wall in the unconfined powder bed with the hot-work tool steel [Fig. 11(a)] and the nickel-base superalloy [Fig. 11(b)]. In these figures, the x- and y-axes show the time and the q-space, while the range adjusted integrated diffraction intensities are represented by the color. In Fig. 11(a), the WAXS signal during an entire layer cycle with the hot-work tool steel is shown, recorded at 10 Hz. The utilized printing parameters were 200 W, 200 mm/s, and a processing temperature of 850 °C. From 18.5 to 21.5 s, a new powder layer (50 µm layer thickness) is fed to the build area by the rake. The rake blades and the powder in front of the rakes induce broad signals when passing the x-ray interaction volume at 20.1 and 21.2 s. The newly recoated cold powder shows a $\{110\}_\alpha$ peak that is present until 25 s, after which all the powder in the x-ray interaction volume is transformed into

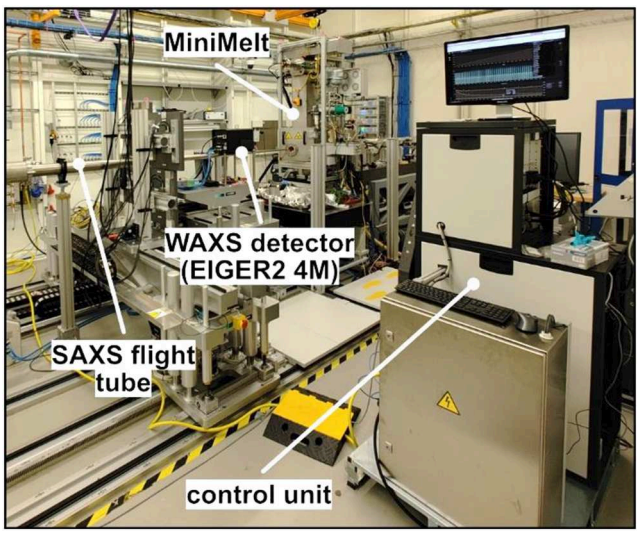

FIG. 10. Combined WAXS and SAXS setup at the P21.2 beamline.

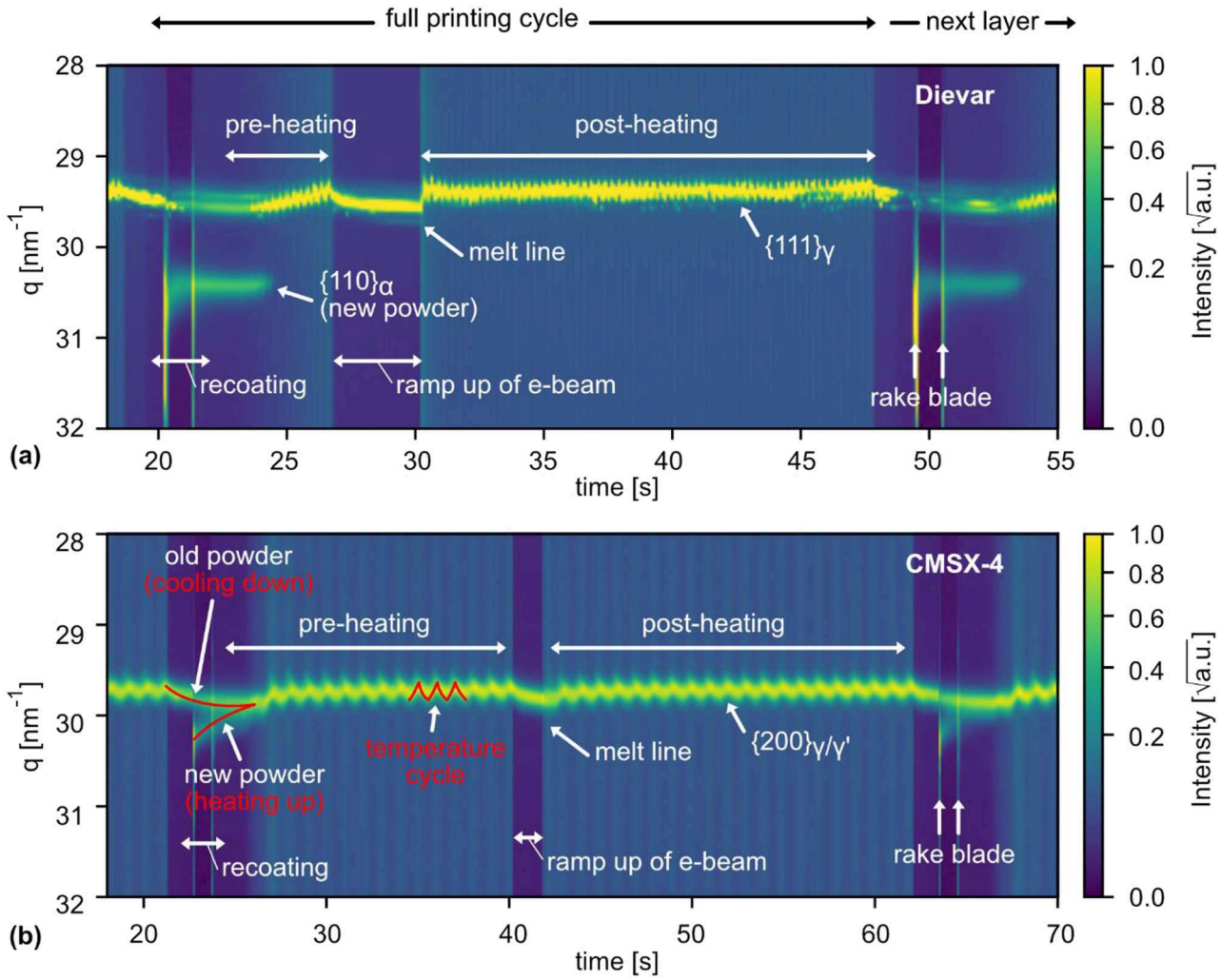

FIG. 11. (a) WAXS data recorded for a full cycle of PBF-EB on the hot-work tool steel powder bed. Starting with recoating of a powder layer (18.5 to 21.5 s), pre-heating (24 to 26.7 s), ramp-up of the beam power (26.7 to 30.2 s), printing of one line (30.2 s), and post-heating (30.2 to 47.8 s). During the powder feed, a phase transformation of the newly recoated powder from α to γ is observed. The beam power was 200 W, and the scanning velocity was 200 mm/s. (b) WAXS data recorded for a full cycle of PBF-EB on the CMSX-4 powder bed. The temperature evolution over one cycle is indicated by the q-value change of the displayed $\{200\}_{\gamma/\gamma'}$-peak. The line was molten at a beam powder of 120 W and a scanning velocity of 50 mm/s.

γ-austenite. The build area is pre-heated from 24 to 26.7 s. During pre-heating, a decrease in the $\{111\}_\gamma$ -peak position is observed, indicating a temperature increase. In the next step, the beam power is ramped up to melting power with the electron beam positioned on the Proheat plate (26.7 to 30.2 s). At 30.2 s, the line of the wall is melted, followed by post-heating until 47.8 s, when the next layer is started by the feeding of new powder. In the recorded WAXS signal, a varying background, introduced by the electron beam—material interaction, is observed, reaching a maximum of ~ 1 % of the maximum peak height when the beam power is highest. For comparison, a similar layer cycle is shown for CMSX-4 powder in Fig. 11(b). Due to the absence of phase transformations in this material over the entire temperature range and due to its lower thermal conductivity, temperature changes are more easily visible. In particular, when fresh powder is supplied to the powder bed, it takes several seconds to heat up, as indicated by the lower q-range of the peak of the supplied powder. Due to the higher processing temperature (> 950 °C), the temperature changes during individual heating cycles are also more pronounced.

In Fig. 12, the melting of a line on the unconfined powder bed recorded at 1 kHz is shown. The hot-work tool steel was melted at 480 W and 300 mm/s. The length of the melted line was 15 mm; hence, it took 50 ms (0.01 to 0.06 s) to melt the line. At 0.035 s, the electron beam passes through the x-ray interaction volume, and the γ-austenite peaks are splitting up. From 0.04 to 0.07 s, a peak of δ-ferrite is present at ~ 30.1 nm^{-1}. The fraction of the γ-austenite

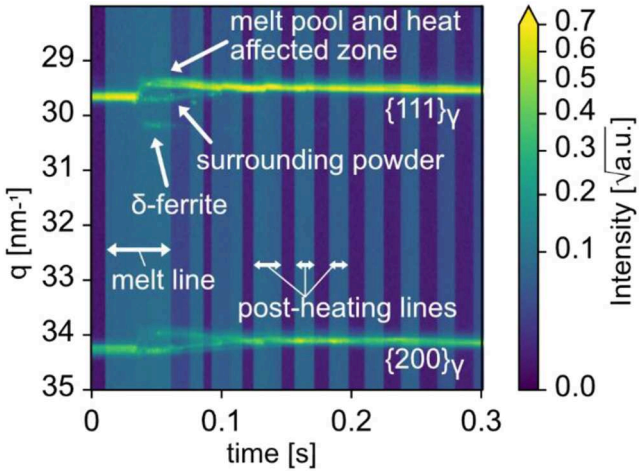

FIG. 12. WAXS recorded during the melting of a line on the unconfined powder bed of the hot-work tool steel and subsequent post-heating patterns recorded at 1 kHz.

peaks exhibiting an increase in q-range after melting is associated with the melt pool and the surrounding heat-affected zone. The fraction exhibiting a continuous decrease is associated with the powder surrounding the melted line. At ~ 0.1 s, both fractions combine again as the temperature homogenizes in the interaction volume. After the melting of the line, the electron beam is scanned over the unconfined powder bed for post-heating. The x-rays created by the electron beam—material interaction during post-heating might be partly shadowed by the powder hill, which would explain the fluctuating background radiation visible from ~ 0.1 to 0.3 s.

Besides the qualitative analysis of the WAXS signal presented here, the WAXS signal recorded during PBF-EB can be utilized to study the solidification, phase transformations, and precipitation quantitatively as well as to investigate the stress state and texture in the solidified material during the build process and the cooling down of the samples after processing.

The SAXS signal can also be recorded and yield information on the evolution of, for example, precipitation. The SAXS signal was recorded during the cooling of the steel samples, but no precipitation has been observed in the performed measurements.

IV. CONCLUSION

We present a PBF-EB sample environment, the MiniMelt, for *in situ* synchrotron measurements of PBF-EB. MiniMelt's design is based on the commercially available Freemelt ONE system (Freemelt AB, Mölndal, Sweden), with the main modification being a reduced process chamber size with integrated x-ray transparent windows. This allows experiments to be developed initially on Freemelt ONE systems, which can then be investigated with MiniMelt in a synchrotron environment, as well as for the transfer of synchrotron results to the Freemelt ONE systems. The software developed for MiniMelt is compatible with standard Freemelt ONE machines as well. Furthermore, we introduce the unconfined powder bed, which allows *in situ* observations of multi-layer builds and provides thermal conditions close to an industrial PBF-EB process. This work describes the characteristics of the equipment and its implementation at the DESY beamlines P61A (radiography) and P21.2 (WAXS and SAXS). The initial results of radiography and WAXS are presented, including measurements of the unconfined powder bed as well as of bulk samples at frame rates up to 15 (radiography) and 1 kHz (WAXS). In the experiments presented, a hot-work tool steel and the Ni-base superalloy CMSX-4 were investigated. The measurements presented showcase the capabilities of the equipment to study the PBF-EB process *in situ*. Moving forward, this equipment will enable the study of the melt pool, powder, and defect dynamics as well as solidification, phase transformation, and precipitation kinetics in PBF-EB. Furthermore, the MiniMelt can be utilized for small-scale electron beam melting as demonstrated for bulk melting of CMSX-4. Other potential applications of the sample environment include the validation and calibration of process monitoring data obtained from the total electron emissions detector, the thermocouples, and other monitoring devices that can be integrated with the equipment.

Ongoing and upcoming experiments with the sample environment are expected to contribute to the progress of PBF-EB by increasing the understanding of the physical phenomena that occur during the various process steps of PBF-EB. The findings of these experiments are anticipated to improve the process and alloy development for PBF-EB. In addition, these experiments can enable and foster model development and validation for PBF-EB.

ACKNOWLEDGMENTS

This work was performed within the project "Real-time tracking of electron beam additive manufacturing," Grant No. 2019-06068, funded by the Swedish Research Council (VR) and the Bundesministerium für Bildung und Forschung (BMBF) via the Röntgen-Ångström Cluster (RÅC). The authors acknowledge DESY (Hamburg, Germany), a member of the Helmholtz Association HGF, for the provision of the synchrotron infrastructure on both beamlines P21.2 and P61A and for the experimental facilities at P21.2, as well as Hereon for the experimental facilities at P61A. We would like to thank Zoltan Hegedues for his assistance during the P21.2 beamtime. Beamtime was allocated for Proposal Nos. II-20220735 EC and I-20220349 EC.

AUTHOR DECLARATIONS

Conflict of Interest

The authors have no conflicts to disclose.

Author Contributions

H.-H.K. and N.S. contributed equally to this work.

Hans-Henrik König: Conceptualization (equal); Investigation (equal); Methodology (equal); Visualization (equal); Writing – original draft (equal); Writing – review & editing (equal). **Nick Semjatov**: Conceptualization (equal); Investigation (equal); Methodology (equal); Software (equal); Writing – original draft (equal); Writing – review & editing (equal). **Gabriel Spartacus**:

Conceptualization (equal); Investigation (equal); Methodology (equal); Visualization (equal); Writing – original draft (supporting); Writing – review & editing (equal). **Pidassa Bidola**: Conceptualization (equal); Investigation (equal); Methodology (equal); Writing – review & editing (supporting). **Chrysoula Ioannidou**: Conceptualization (equal); Investigation (equal); Methodology (equal); Writing – original draft (supporting); Writing – review & editing (supporting). **Jihui Ye**: Investigation (supporting); Software (equal); Writing – review & editing (supporting). **Jakob Renner**: Investigation (supporting); Software (equal); Writing – review & editing (supporting). **Ulrich Lienert**: Conceptualization (equal); Funding acquisition (supporting); Investigation (supporting); Methodology (equal); Writing – review & editing (supporting). **Guilherme Abreu Faria**: Conceptualization (equal); Investigation (supporting); Methodology (equal); Writing – review & editing (supporting). **Benjamin Wahlmann**: Conceptualization (equal); Investigation (equal); Methodology (equal); Writing – review & editing (supporting). **Martin Wildheim**: Conceptualization (equal); Investigation (supporting); Methodology (equal); Writing – review & editing (supporting). **Ulf Ackelid**: Conceptualization (equal); Methodology (equal); Writing – review & editing (supporting). **Felix Beckmann**: Conceptualization (equal); Funding acquisition (supporting); Methodology (equal); Supervision (lead); Writing – review & editing (supporting). **Peter Staron**: Conceptualization (equal); Methodology (equal); Project administration (lead); Writing – review & editing (supporting). **Peter Hedström**: Conceptualization (equal); Funding acquisition (supporting); Methodology (equal); Supervision (supporting); Writing – review & editing (supporting). **Carolin Körner**: Conceptualization (equal); Funding acquisition (lead); Methodology (equal); Project administration (lead); Supervision (lead); Writing – review & editing (supporting). **Greta Lindwall**: Conceptualization (equal); Funding acquisition (lead); Methodology (equal); Project administration (lead); Supervision (lead); Writing – original draft (supporting); Writing – review & editing (supporting).

DATA AVAILABILITY

The data that support the findings of this study are available from the corresponding authors upon reasonable request.

REFERENCES

[1] C. Körner, "Additive manufacturing of metallic components by selective electron beam melting—A review," Int. Mater. Rev. **61**(5), 361–377 (2016).

[2] C. Botero, M. Ramsperger, A. Selte, K. Åsvik, A. Koptyug, P. Skoglund, S. Roos, L. E. Rännar, and M. Bäckström, "Additive manufacturing of a cold-work tool steel using electron beam melting," Steel Res. Int. **91**(5), 1900448 (2020).

[3] P. Fernandez-Zelaia, C. Ledford, E. A. I. Ellis, Q. Campbell, A. M. Rossy, D. N. Leonard, and M. M. Kirka, "Crystallographic texture evolution in electron beam melting additive manufacturing of pure Molybdenum," Mater. Des. **207**, 109809 (2021).

[4] L. M. Sochalski-Kolbus, E. A. Payzant, P. A. Cornwell, T. R. Watkins, S. S. Babu, R. R. Dehoff, M. Lorenz, O. Ovchinnikova, and C. Duty, "Comparison of residual stresses in Inconel 718 simple parts made by electron beam melting and direct laser metal sintering," Metall. Mater. Trans. A **46**(3), 1419–1432 (2015).

[5] H. L. Wei, T. Mukherjee, W. Zhang, J. S. Zuback, G. L. Knapp, A. De, and T. DebRoy, "Mechanistic models for additive manufacturing of metallic components," Prog. Mater. Sci. **116**, 100703 (2021).

[6] T. DebRoy, H. L. Wei, J. S. Zuback, T. Mukherjee, J. W. Elmer, J. O. Milewski, A. M. Beese, A. Wilson-Heid, A. De, and W. Zhang, "Additive manufacturing of metallic components–Process, structure and properties," Prog. Mater. Sci. **92**, 112–224 (2018).

[7] Z. Fu and C. Körner, "Actual state-of-the-art of electron beam powder bed fusion," Eur. J. Mater. **2**(1), 54–116 (2022).

[8] C. Körner, M. Markl, and J. A. Koepf, "Modeling and simulation of microstructure evolution for additive manufacturing of metals: A critical review," Metall. Mater. Trans. A **51**(10), 4970–4983 (2020).

[9] C. Ioannidou, H.-H. König, N. Semjatov, U. Ackelid, P. Staron, C. Körner, P. Hedström, and G. Lindwall, "In-situ synchrotron X-ray analysis of metal additive manufacturing: Current state, opportunities and challenges," Mater. Des. **219**, 110790 (2022).

[10] Q. Guo, C. Zhao, M. Qu, L. Xiong, S. M. H. Hojjatzadeh, L. I. Escano, N. D. Parab, K. Fezzaa, T. Sun, and L. Chen, "In-situ full-field mapping of melt flow dynamics in laser metal additive manufacturing," Addit. Manuf. **31**, 100939 (2020).

[11] Y. Huang, T. G. Fleming, S. J. Clark, S. Marussi, K. Fezzaa, J. Thiyagalingam, C. L. A. Leung, and P. D. Lee, "Keyhole fluctuation and pore formation mechanisms during laser powder bed fusion additive manufacturing," Nat. Commun. **13**(1), 1170 (2022).

[12] N. Kouraytem, P.-J. J. Chiang, R. Jiang, C. Kantzos, J. Pauza, R. Cunningham, Z. Wu, G. Tang, N. Parab, C. Zhao, K. Fezzaa, T. Sun, and A. D. Rollett, "Solidification crack propagation and morphology dependence on processing parameters in AA6061 from ultra-high-speed x-ray visualization," Addit. Manuf. **42**, 101959 (2021).

[13] G. Graf, J. Rosigkeit, E. Krohmer, P. Staron, R. Krenn, H. Clemens, and P. Spoerk-Erdely, "In situ investigation of the rapid solidification behavior of intermetallic γ-TiAl-based alloys using high-energy X-ray diffraction," Adv. Eng. Mater. **23**(11), 2100557 (2021).

[14] J. A. Glerum, S. Hocine, C. S. T. Chang, C. Kenel, S. Van Petegem, N. Casati, D. F. Sanchez, H. Van Swygenhoven, D. C. Dunand, and D. C. Dunand, "Operando X-ray diffraction study of thermal and phase evolution during laser powder bed fusion of Al-Sc-Zr elemental powder blends," Addit. Manuf. **55**, 102806 (2022).

[15] B. Wahlmann, E. Krohmer, C. Breuning, N. Schell, P. Staron, E. Uhlmann, and C. Körner, "In situ observation of γ′phase transformation dynamics during selective laser melting of CMSX-4," Adv. Eng. Mater. **23**(11), 2100112 (2021).

[16] F. Schmeiser, E. Krohmer, N. Schell, E. Uhlmann, and W. Reimers, "Internal stress evolution and subsurface phase transformation in titanium parts manufactured by laser powder bed fusion—An in situ X-ray diffraction study," Adv. Eng. Mater. **23**(11), 2001502 (2021).

[17] S. Hocine, H. Van Swygenhoven, and S. Van Petegem, "Verification of selective laser melting heat source models with *operando* X-ray diffraction data," Addit. Manuf. **37**, 101747 (2021).

[18] B. Schneiderman, A. C. Chuang, P. Kenesei, and Z. Yu, "In situ synchrotron diffraction and modeling of non-equilibrium solidification of a MnFeCoNiCu alloy," Sci. Rep. **11**(1), 5921 (2021).

[19] D. Tourret, J. Klemm-Toole, A. E. Castellanos, B. Rodgers, G. Becker, A. Saville, B. Ellyson, C. Johnson, B. Milligan, J. Copley, R. Ochoa, A. Polonsky, K. Pusch, M. P. Haines, K. Fezzaa, T. Sun, K. Clarke, S. Babu, T. Pollock, A. Karma, and A. Clarke, "Morphological stability of solid-liquid interfaces under additive manufacturing conditions," Acta Mater. **250**, 118858 (2023).

[20] H.-H. König, N. H. Pettersson, A. Durga, S. Van Petegem, D. Grolimund, A. C. Chuang, Q. Guo, L. Chen, C. Oikonomou, F. Zhang, and G. Lindwall, "Solidification modes during additive manufacturing of steel revealed by high-speed X-ray diffraction," Acta Mater. **246**, 118713 (2023).

[21] L. I. Escano, S. J. Clark, A. C. Chuang, J. Yuan, Q. Guo, M. Qu, W. Dong, X. Zhang, J. Huang, K. Fezzaa, P. Kenesei, B. J. Walker, T. Sun, K. W. Eliceiri, and L. Chen, "An electron beam melting system for in-situ synchrotron X-ray monitoring," Addit. Manuf. Lett. **3**, 100094 (2022).

[22] C. Zhao, K. Fezzaa, R. W. Cunningham, H. Wen, F. De Carlo, L. Chen, A. D. Rollett, and T. Sun, "Real-time monitoring of laser powder bed fusion

process using high-speed X-ray imaging and diffraction," Sci. Rep. **7**(1), 3602 (2017).
[23]N. P. Calta, J. Wang, A. M. Kiss, A. A. Martin, P. J. Depond, G. M. Guss, V. Thampy, A. Y. Fong, J. N. Weker, K. H. Stone, C. J. Tassone, M. J. Kramer, M. F. Toney, A. Van Buuren, and M. J. Matthews, "An instrument for *in situ* time-resolved X-ray imaging and diffraction of laser powder bed fusion additive manufacturing processes," Rev. Sci. Instrum. **89**(5), 055101 (2018).
[24]C. L. A. Leung, S. Marussi, M. Towrie, J. del Val Garcia, R. C. Atwood, A. J. Bodey, J. R. Jones, P. J. Withers, and P. D. Lee, "Laser-matter interactions in additive manufacturing of stainless steel SS316L and 13-93 bioactive glass revealed by *in situ* X-ray imaging," Addit. Manuf. **24**, 647–657 (2018).
[25]E. Uhlmann, E. Krohmer, F. Schmeiser, N. Schell, and W. Reimers, "A laser powder bed fusion system for *in situ* x-ray diffraction with high-energy synchrotron radiation," Rev. Sci. Instrum. **91**(7), 075104 (2020).
[26]S. Hocine, S. Van Petegem, U. Frommherz, G. Tinti, N. Casati, D. Grolimund, and H. Van Swygenhoven, "A miniaturized selective laser melting device for *operando* X-ray diffraction studies," Addit. Manuf. **34**, 101194 (2020).
[27]U. Ackelid, U.S. patent 2023/0150201 A1 (18 May 2023).
[28]C. Ledford, M. Tung, C. Rock, and T. Horn, "Real time monitoring of electron emissions during electron beam powder bed fusion for arbitrary geometries and toolpaths," Addit. Manuf. **34**, 101365 (2020).
[29]J. Bäreis, N. Semjatov, J. Renner, J. Ye, F. Zongwen, and C. Körner, "Electron-optical in-situ crack monitoring during electron beam powder bed fusion of the Ni-Base superalloy CMSX-4," Prog. Addit. Manuf. **8**, 801 (2022).
[30]J. Ye, J. Renner, C. Körner, and Z. Fu, "Electron-optical observation of smoke evolution during electron beam powder bed fusion," Addit. Manuf. **70**, 103578 (2023).
[31]C. Breuning, J. Pistor, M. Markl, and C. Körner, "Basic mechanism of surface topography evolution in electron beam based additive manufacturing," Materials **15**(14), 4754 (2022).
[32]P. M. Bidola, G. Abreu-Faria, J. Klingenberg, J. Brehling, H. Burmesterm, U. Tietze, C. Krywka, P. Staron, B. Schwebke, L. Lottermoser, G. Lindwall, C. Ioannidou, H.-H. König, G. Spartacus, N. Semjatov, and F. Beckmann, Proc. SPIE **12694**, 1269402 (2023).
[33]G. Ashiotis, A. Deschildre, Z. Nawaz, J. P. Wright, D. Karkoulis, F. E. Picca, and J. Kieffer, "The fast azimuthal integration Python library:*pyFAI*," J. Appl. Crystallogr. **48**(2), 510–519 (2015).